AIAA 2003–0263

Detached-Eddy Simulation around a Forebody at High Angle of Attack

Aroon K. Viswanathan
MAE Department, Arizona State University, Tempe, AZ

Kory R. Klismith, James R. Forsythe
United States Air Force Academy, Colorado Springs, CO

Kyle D. Squires
MAE Department, Arizona State University, Tempe, AZ

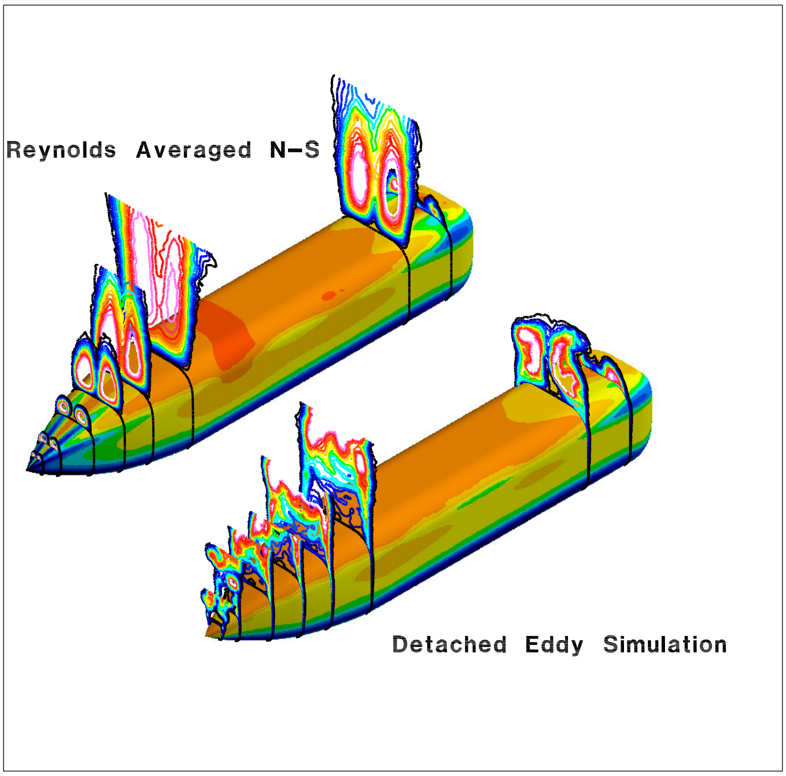

Aerospace Sciences Meeting 2003
6–9 January 2003 / Reno, Nevada

Detached-Eddy Simulation around a Forebody at High Angle of Attack

Aroon K. Viswanathan*
MAE Department, Arizona State University, Tempe, AZ
Kory R. Klismith† James R. Forsythe‡
United States Air Force Academy, Colorado Springs, CO
Kyle D. Squires§
MAE Department, Arizona State University, Tempe, AZ

Predictions of the massively separated flow around a rectangular ogive forebody are obtained using Detached-Eddy Simulation (DES) and solutions of the unsteady Reynolds-averaged Navier-Stokes (URANS) equations. Based on the body width/diameter D, the forebody length is $2D$ while the length of the aft section is $4D$. The cross-section is a rounded-corner square with corner radius $D/4$. The angle of attack of the freestream is 90°, the Reynolds number based on freestream speed and diameter is 2.1×10^6, and the freestream Mach number is 0.21. Computations of the static geometry and of the ogive undergoing prescribed rotary motion are performed on unstructured meshes with cell sizes ranging from 2.1×10^6 to 8.8×10^6 cells comprised of prisms and tetrahedra. Predictions of the flow with fully turbulent boundary layers are obtained via prescription of a small level of eddy viscosity at the inlet to the computational domain. Separation occurs off the rear portion of the ogive with the subsequent development in the DES of a chaotic and three-dimensional wake. Flow visualizations demonstrate an increase in the range of resolved scales with grid refinement. Time-averaged drag predictions for the static geometry show adequate grid convergence. DES predictions of the pressure distribution at axial stations along the ogive are also in good agreement with measured values. URANS predictions of the pressure along the forebody exhibit relatively strong coherence, with the resulting pressure varation substantially different from the measured values and DES results. The computation with rotary motion is performed at a spin coefficient of 0.2, predictions of the pressure distribution around the forebody for this case exhibit adequate agreement with measured values.

Introduction

THE flowfields encountered around fighter aircraft at high angles of attack comprise a technologically important regime, e.g., as relates to stability and control. Predictive methodologies that can be used to study flow characteristics in flight regimes are important tools for analysis and, ultimately, design. An example relevant to the present effort are flows encountered in rotary motions characteristic of an aircraft spin. A crucial region in predicting spin characteristics of modern fighters is the forebody, imposing a relatively long moment arm and characterized by complex vortical flows. These features challenge computational approaches, especially at high angle of attack for which regions of massive flow separation are encountered. In addition, the Reynolds numbers in flight regimes are high, a fact that imposes additional constraints on predictive strategies.

*Research Assistant
†Cadet First Class
‡AIAA Senior Member, present affiliation: Cobalt Solutions LLC
§Professor, AIAA Member

Lab experiments and flight tests are two methods to investigating flowfield characteristics at flight Reynolds numbers. Computational Fluid Dynamics (CFD) offers a useful tool that can complement existing approaches by enabling, for example, efficient consideration of several configurations, an ability to study in detail various aspects of a design, etc. While promising, the performance of CFD has traditionally been uneven in accurately predicting high Reynolds number turbulent flows with massive separation.

Most high-Reynolds number predictions are obtained from solutions of the Reynolds-averaged Navier-Stokes (RANS) equations. While the most popular RANS models appear to yield predictions of useful accuracy in attached flows as well as some with shallow separations, RANS predictions of massively separated flows have typically been unreliable. RANS models, calibrated in thin shear layers, appear unable to consistently represent to sufficient accuracy the geometry-dependent, chaotic and unsteady features of massive separations.

The relatively poor performance of RANS models has motivated the increased application of Large Eddy Simulation (LES). Away from solid surfaces, LES is a powerful approach, providing a description of the large, energy-containing scales of motion that are typically dependent on geometry and boundary conditions. When applied to boundary layers, however, the computational cost of whole-domain LES does not differ significantly from that of Direct Numerical Simulation (DNS) [1].

In the present contribution, predictions are obtained using Detached-Eddy Simulation (DES), a hybrid method which has RANS behavior near the wall and becomes a Large Eddy Simulation in the regions away from solid surfaces provided the grid density is sufficient [1]. The formulation used in the present contribution is based on a modification to the Spalart-Allmaras one-equation model [2], referred to as S-A throughout and described in greater detail in the next section. DES is a non-zonal technique that is computationally feasible for high Reynolds number prediction, but also resolves time-dependent, three-dimensional turbulent motions as in LES. Previous applications of the method have been favorable, yielding adequate predictions across a range of flows and also showing the computational cost has a weak dependence on Reynolds number, similar to RANS methods yet at the same time providing more realistic descriptions of unsteady effects (see also Strelets [3]).

The present study is a part of a larger application in which the aim is prediction of the spin characteristics of full aircraft at flight Reynolds numbers, recent progress in that area is also reported at this meeting [4]. Thus, in addition to computation of the flow around the static geometry, an additional aim of the work is prediction of the flow field around the ogive undergoing rotary motion. The flow fields are massively separated and are a "natural" application of DES. Though a natural application for the model, calculations of complex configurations at high Reynolds numbers challenge the entire computational approach. Assessment of the grid, for example, is important to establishing the method and one of the goals of the work is to explore the influence of the mesh on DES predictions. This is not a simple matter of verifying the order of accuracy, which is difficult to define and predict in LES and especially hybrid methods. The primary tool for such a study remains grid refinement.

The flow considered is that around a rectangular ogive forebody, cross-sections are shown in Figure 1. The length of the aft section is four times the width ("diameter", D), the cross-section being a rounded-corner square in which the corner radius is 1/4 of the width (similar to the cross-sections of the X-29 and T-38) and with a hemispherical endcap. The length of the forebody (ogive cone) is twice the diameter, with a similar cross-section as the main body.

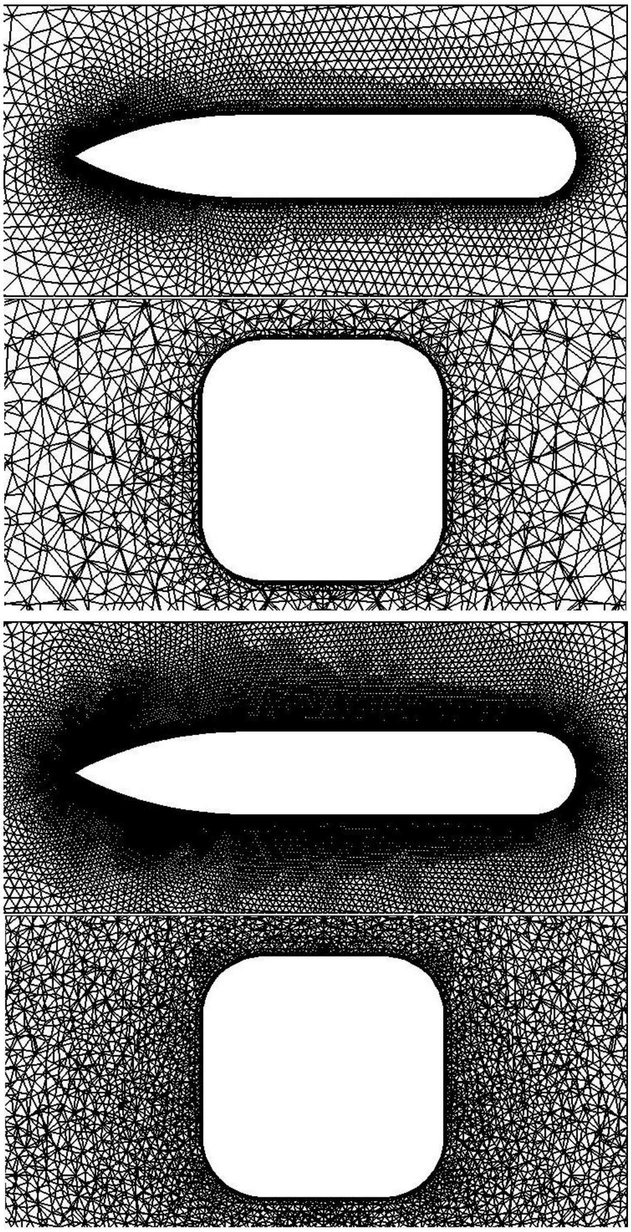

Fig. 1 Side and end views of the coarse and fine grids. Length of the forebody ogive = $2D$, total length = $6D$. Cross-section is a square with rounded corners, radius = $D/4$.

Background

Rotary balance experiments on circular and square ogive bodies were reported by Pauley *et al.* [5]. An extensive database was established with Reynolds number variation accomplished using a pressurized wind tunnel. The forebodies were at high angle of attack, $\alpha = 60°$ and $90°$. The Reynolds number variation was from 8×10^4 to 2.25×10^6 (based on the freestream speed and diameter D). These investigators reported force and moment measurements along with pressure distributions at axial stations along the bodies for static geometries as well as for cases with prescribed rotation. For the cases with rotation, the spin coefficient $\Omega L/(2U_\infty)$ was varied by as much as ± 0.4.

Pauley *et al.* [5] found that flow attachment along the forebody was correlated to the local Reynolds number, which varied with width, measurements showing that $Re > 2 \times 10^5$ was required for attached flow on the forebody. Flowfield characteristics exhibited a relatively strong dependence on Reynolds number up to around 5×10^5. For cases with rotary motion, the side force and yawing moment did not exhibit the same characteristics as for the static case. van Dam *et al.* [6] computed the flow around the rectangular ogive at 60° angle of attack and for a spin coefficient of 0.2. Most of the solutions of the unsteady RANS (URANS) equations were obtained using the Baldwin-Lomax model with additional calculations performed using S-A. In general, reasonable agreement between measured and predicted pressure distributions was reported.

Approach

Detached Eddy Simulation

The DES formulation employed in this work is based on a modification to the Spalart-Allmaras RANS model [2] such that the model reduces to its RANS formulation near solid surfaces and to a subgrid model away from the wall [1]. The Spalart-Allmaras RANS model solves an equation for the variable $\tilde{\nu}$ which is dependent on the turbulent viscosity. The model is derived based on empiricism and arguments of Galilean invarience, dimensional analysis and dependence on molecular viscosity. The model includes a wall destruction term that reduces the turbulent viscosity in the laminar sub-layer and trip terms to provide smooth transition to turbulence. The transport equation for the working variable $\tilde{\nu}$ used to form the eddy viscosity takes the form,

$$\begin{aligned} \frac{D\widetilde{\nu}}{Dt} &= c_{b1}\widetilde{S}\,\widetilde{\nu} - \left[c_{w1}f_w - \frac{c_{b1}}{\kappa^2}f_{t2}\right]\left[\frac{\widetilde{\nu}}{d}\right]^2 \\ &+ \frac{1}{\sigma}\left[\nabla\cdot((\nu+\widetilde{\nu})\nabla\widetilde{\nu}) + c_{b2}\,(\nabla\widetilde{\nu})^2\right], \quad (1) \end{aligned}$$

where $\widetilde{\nu}$ is the working variable. The eddy viscosity ν_t is obtained from,

$$\nu_t = \widetilde{\nu}\, f_{v1} \qquad f_{v1} = \frac{\chi^3}{\chi^3 + c_{v1}^3} \qquad \chi \equiv \frac{\widetilde{\nu}}{\nu} \qquad (2)$$

where ν is the molecular viscosity. The production term is expressed as,

$$\widetilde{S} \equiv S + \frac{\widetilde{\nu}}{\kappa^2 d^2} f_{v2}\,, \qquad f_{v2} = \left(1 + \frac{\chi}{c_{v2}}\right)^{-3}, \qquad (3)$$

where S is the magnitude of the vorticity. The function f_w is given by,

$$\begin{aligned} f_w &= g\left[\frac{1 + c_{w3}^6}{g^6 + c_{w3}^6}\right]^{1/6} \\ g &= r + c_{w2}\,(r^6 - r) \\ r &\equiv \frac{\widetilde{\nu}}{\widetilde{S}\kappa^2 d^2}\,. \end{aligned} \qquad (4)$$

The wall boundary condition is $\widetilde{\nu} = 0$. The constants are $c_{b1} = 0.1355$, $\sigma = 2/3$, $c_{b2} = 0.622$, $\kappa = 0.41$, $c_{w1} = c_{b1}/\kappa^2 + (1 + c_{b2})/\sigma$, $c_{w2} = 0.3$, $c_{w3} = 2$, $c_{v1} = 7.1$, $c_{v2} = 5$, $c_{t1} = 1$, $c_{t2} = 2$, $c_{t3} = 1.1$, and $c_{t4} = 2$.

The DES formulation is obtained by replacing in the S-A model the distance to the nearest wall, d, by $\widetilde{d}$, where $\widetilde{d}$ is defined as,

$$\widetilde{d} \equiv \min(d, C_{DES}\Delta)\,. \qquad (5)$$

In (5), Δ is the largest distance between the cell center under consideration and the cell center of the neighbors (i.e., those cells sharing a face with the cell in question). In "natural" applications of DES, the wall-parallel grid spacings (e.g., streamwise and spanwise) are on the order of the boundary layer thickness and the S-A RANS model is retained throughout the boundary layer, i.e., $\widetilde{d} = d$. Consequently, prediction of boundary layer separation is determined in the "RANS mode" of DES. Away from solid boundaries, the closure is a one-equation model for the sub-grid scale eddy viscosity. When the production and destruction terms of the model are balanced, the length scale $\widetilde{d} = C_{DES}\Delta$ in the LES region yields a Smagorinsky-like eddy viscosity $\widetilde{\nu} \propto S\Delta^2$. Analogous to classical LES, the role of Δ is to allow the energy cascade down to the grid size. The additional model constant $C_{DES} = 0.65$ was set in homogeneous turbulence[7].

Flow solver and grid

The compressible Navier-Stokes equations are solved on unstructured grids using Cobalt [8], a commercial version of Cobalt$_{60}$, the Navier-Stokes solver developed at the Air Force Research Laboratory. The numerical method is a cell-centered finite volume approach applicable to arbitrary cell topologies (e.g, hexahedrons, prisms, tetrahedrons). The spatial operator uses the exact Riemann Solver of Gottlieb and Groth[9], least squares gradient calculations using QR factorization to provide second order accuracy in space, and TVD flux limiters to limit extremes at cell faces. A point implicit method using analytic first-order inviscid and viscous Jacobians is used for advancement of the discretized system. For time-accurate computations, a Newton sub-iteration scheme is employed, the method is second order accurate in time. The domain decomposition library ParMETIS [10] is used for parallel implementation and provides optimal load balancing with a minimal surface interface between zones. Communication between processors is achieved using Message Passing Interface.

Calculations were carried out on a cubic domain that extends from the origin, located at the centroid

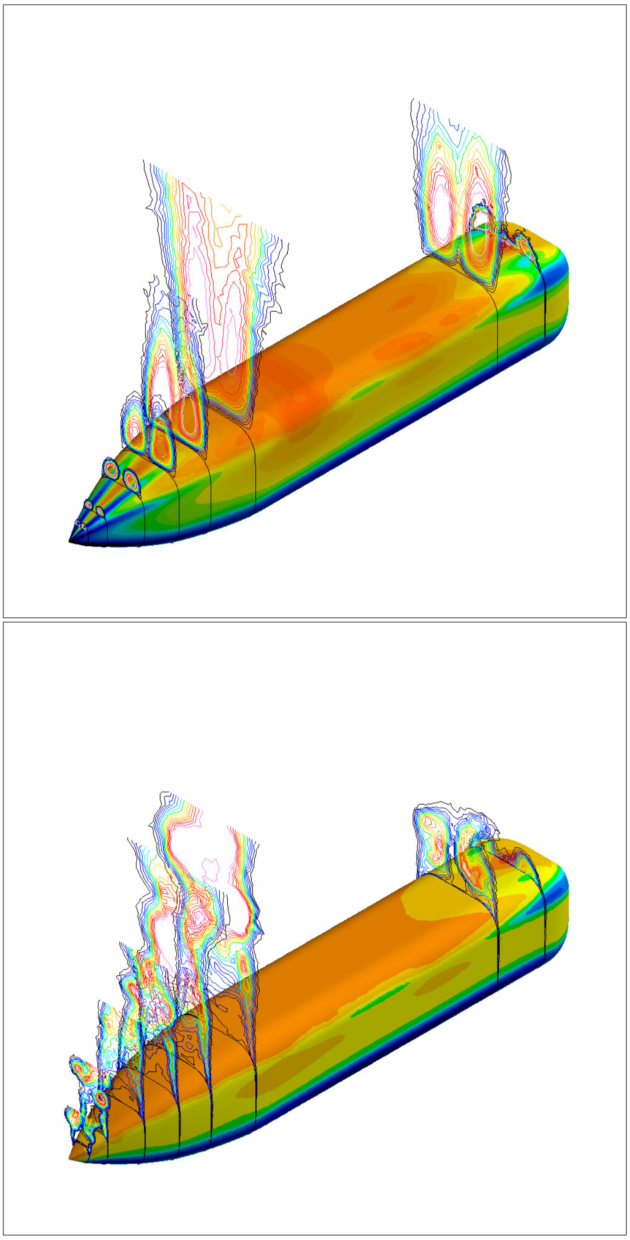

Fig. 2 Ratio of the instantaneous eddy viscosity to the molecular value at the eight axial locations for which pressure measurements are available. Upper frame: URANS; lower frame: DES. Geometry colored by pressure.

of the ogive, to around 10 times the ogive length. The computations were performed on unstructured grids generated using VGRIDns [11]. The grid was clustered near the ogive surface and geometrically stretched at a rate of 1.2 away from the wall, the distance from the wall to the first cell center was less than $2 \times 10^{-6} D$, within one viscous unit on average. In addition, the grid was clustered in the vicinity of the forebody tip in attempt to accurately capture solution variations in that region.

Grid refinement was accomplished via variation of the parameter *ifact* in VGRIDns, enabling an efficient and uniform refinement in all directions. Computations were performed on a series of four grids, a baseline mesh comprised of approximately 6.5×10^6 cells, a fine grid with around 8.75×10^6 cells, and two coarser meshes comprised of approximately 2.1×10^6 cells (coarse) and 3.5×10^6 cells. Cross sections showing the coarse and fine grids are shown in Figure 1. Defining a flow timescale using the ogive diameter D and freestream speed, DES predictions on the baseline grid were sampled for over 100 time units, the dimensionless timestep was 0.025.

Results

Flow structure – static geometry

Shown in Figure 2 are contours of the eddy viscosity ratio along the ogive at the eight axial stations for which pressure measurements are avaiable for assessing simulation results. The ogive surface is colored by the instantaneous pressure in Figure 2. On the lee side, the URANS prediction shows that the wake is comprised of a pair of counter-rotating coherent vortical motions, as evidenced by the contours of the eddy viscosity in the planes and the signature of these structures on the surface pressure, especially along the forebody. The DES prediction, on the other hand, exhibits a more chaotic structure in the planes along the forebody. Also apparent is the more uniform pressure on the leeward surface of the forebody, the figure showing a marked difference compared to the URANS result.

One effect of mesh refinement is shown in Figure 3 where contours of the instantaneous vorticity magnitude are shown in the center plane $x/L = 0.5$ for the coarse, baseline, and fine grids as well as the RANS result (bottom frame), which was obtained on the baseline grid. In general, and analogous to the behavior observed in other DES predictions of bluff-body flows [12], increases in mesh density lead to a wider range of scales resolved in the wake. The fine-grid result shows substantially more eddy content than captured in the coarse-grid DES prediction, the result obtained on the baseline mesh appears to possess an adequate range of scales. The URANS result in the lowest frame shows relatively short shear layers that are diffused in the near wake, the structure of the coarse-grid DES prediction (top frame) is somewhat similar to that of the URANS.

Another view of mesh refinement is provided in Figure 4 in which contours of the instantaneous vorticity magnitude are shown in plane normal to the freestream flow, in the wake of the ogive one-half diameter downstream of the rear surface. The DES predictions, and to a lesser extent the URANS result, show a tapering of the wake towards the forebody. Figure 4 also shows that, moving from the top to the third frame, refinement of the grid leads to a wider range of scales in the wake. For the plane shown, the DES solutions exhibit substantial variation along the axial ("spanwise") co-

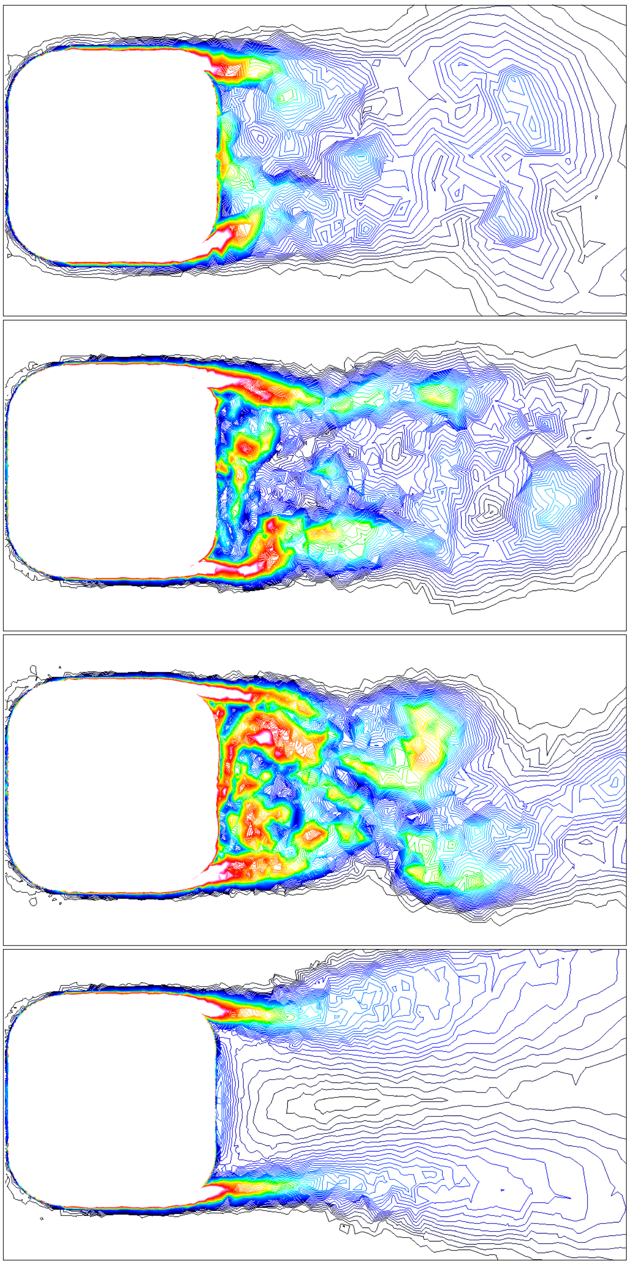

Fig. 3 Contours of the instantaneous vorticity magnitude at the center of the ogive, $x/L = 0.5$. Upper frame: coarse grid; second frame from top: baseline grid; third frame from top: fine grid; bottom frame: URANS (baseline grid).

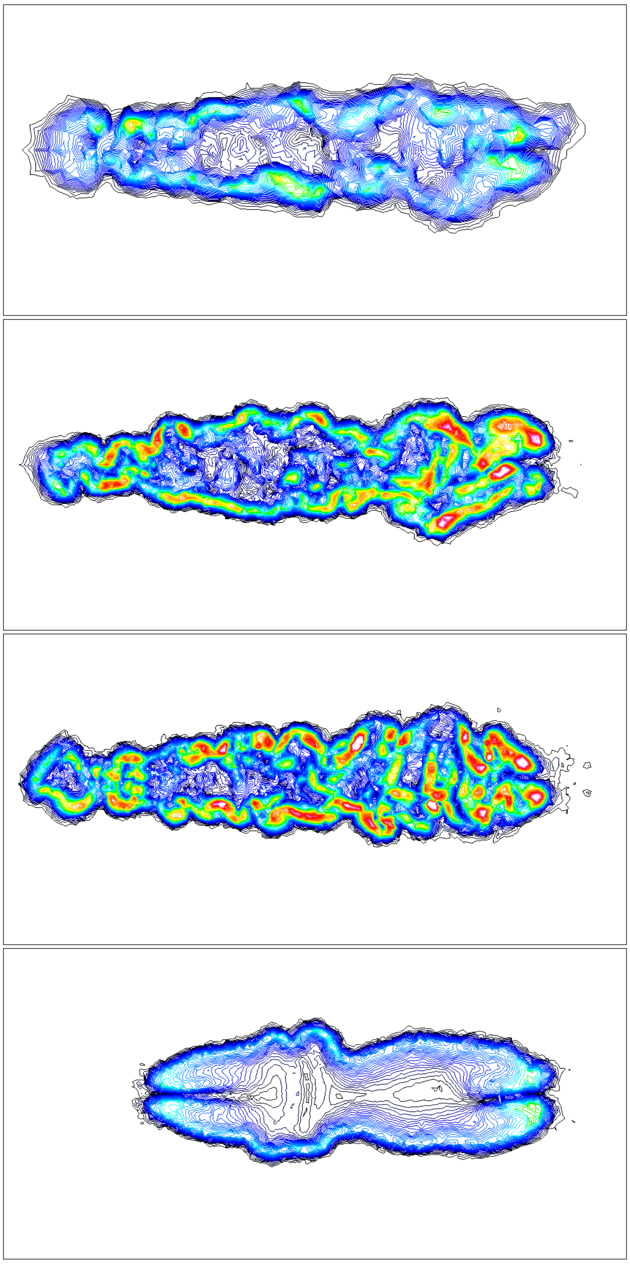

Fig. 4 Contours of the instantaneous vorticity magnitude in the plane $y = D/2$, view is normal to the freestream velocity. Upper frame: coarse grid; second frame from top: baseline grid; third frame from top: fine grid; bottom frame: URANS (baseline grid).

ordinate. Axial varation is captured to a lesser extent in the URANS result.

Force and moment histories

Shown in Figure 5 are DES and URANS predictions of the time histories of the forces and yawing moment for simulations performed using the baseline grid. In general, the temporal variation in the forces and yawing moment from the URANS is substantially lower than achieved in the DES. As shown in the figure, the streamwise (drag) force from the URANS, while for the most part consistently higher than the DES result, does not differ drastically from the DES with the averaged drag coefficient from the URANS prediction at 0.334, that for the DES on the baseline grid is 0.321. The three-dimensionality developed in the URANS, while not as pronounced as in the DES (c.f., Figure 2) seems sufficient such that the structural features affecting the drag can be taken into account. The variations in the mean drag and mean axial force along with the rms values of the side force and yawing moment are summarized in Table 1 and Table 2. As shown in Table 1, the range in the averaged drag for

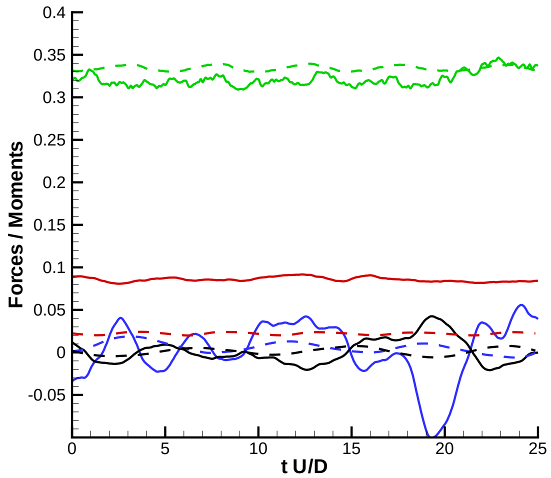

Fig. 5 DES and URANS predictions of force and yawing moment histories, baseline grid. Solid lines represent DES, dashed lines represent URANS case. Green: streamwise (drag) force; red: axial force; blue: lateral (side) force; black: yawing moment.

Case	axial force	streamwise force
DES coarse	0.0830	0.3244
DES baseline	0.0857	0.3212
DES fine	0.0853	0.3217
URANS baseline	0.022	0.334

Table 1 Mean axial and drag force.

the DES predictions for the grid resolutions considered was not large, varying between 0.321 and 0.325.

The development of the side force and yawing moment in Figure 5 between the DES and URANS exhibit similar features, with substantially larger variation with time in the DES predictions compared to the URANS result. The largest differences in forces occurs in prediction of the axial value (aligned with the long axis of the ogive). As shown in Figure 5, the axial force from the DES is substantially larger, nearly a factor of four in the mean, as compared to the URANS (see also Table 1). The difference arises because of the changes in flow structure illustrated previously. Figure 2, for example, show that the DES prediction of the pressure distribution over the leeward side of the ogive is more uniform compared to the URANS. As shown below, the overall pressure along the forebody section is higher than achieved in the URANS, leading in Figure 5 to a larger axial force compared to URANS. Table 2 shows that the rms levels are about five times smaller than obtained in the DES predictions.

Case	side force (rms)	yawing moment (rms)
DES coarse	0.031	0.016
DES baseline	0.035	0.020
DES fine	0.037	0.019
URANS baseline	0.0068	0.0043

Table 2 Rms side force and yawing moment.

Pressure distributions

Pressure distributions around the ogive were measured at eight axial stations, six along the forebody, at $x/L = 0.027, 0.055, 0.111, 0.166, 0.222, 0.305$ and two stations on the aftbody at $x/L = 0.805$ and 0.903. In the pressure distributions reported below, the angle θ is measured positive clockwise from the windward symmetry plane. Comparions of DES and URANS predictions of the pressure variation at the eight axial stations for the static-geometry (non-rotating) ogive are shown in Figures 6-13. From the stagnation point at $\theta = 0°$, the experimental measurements indicate that the flow along the forebody sections is attached. Minima in the pressure coefficient are measured in the vicinity $\theta = 48° - 56°$ and $\theta = 303° - 310°$ as the flow accelerates around the windward corners of the forebody. Comparison of Figures 6-Figure 11 shows that the magnitudes of the suction are mostly constant, with minimum C_p around -2.25 to -2.50.

Another pair of suction minima in C_p are observed as the flow negotiates the corners on the leeward side at angles $\theta = 118° - 120°$ and $\theta = 240° - 242°$. These secondary minima are more pronounced from Station 1 ($x/L = 0.027$) to Station 8 ($x/L = 0.903$). At the last two axial stations, the pressure coefficients near the leeward corners are comparable in magnitude to the suction maxima at the windward, this effect arising to the presence of the endcap. On the forebody, separation is predicted at $\theta = 127° - 132°$ and $\theta = 229° - 232°$, with the measured C_p uniform in the separated region on the forebody.

DES predictions of C_p are in generally good agreement with the experimental measurements, especially along the forebody with the exception of the first station (Figure 6) where the DES minima is not as deep as that measured. As shown in Figure 14, there is convergence towards the measured pressure with grid refinement. Importantly, the establishment of fully turbulent boundary layers as the fluid contacts the ogive surface maintains attached flow around the windward corners, as shown in Figures 7-11, the agreement between DES predictions and the experimental measurements is excellent. URANS predictions of the pressure coefficient on the forebody are noticeably poor, exhibiting significant variation with θ due to the coherent structure that is prediction in the leeward region (c.f., Figure 2).

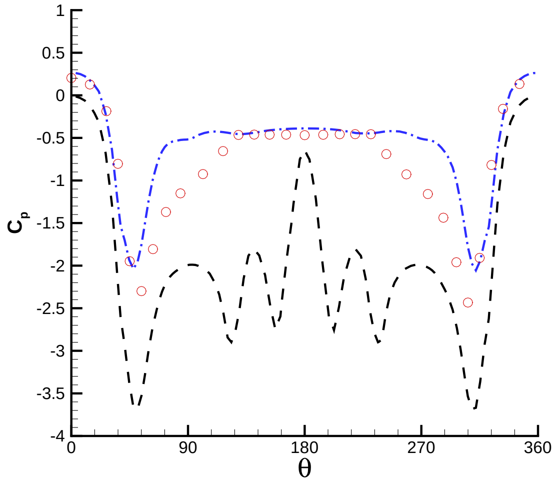

Fig. 6 Pressure coefficient at $x/L = 0.027$. **∘ measurements; —·— DES; ---- URANS.**

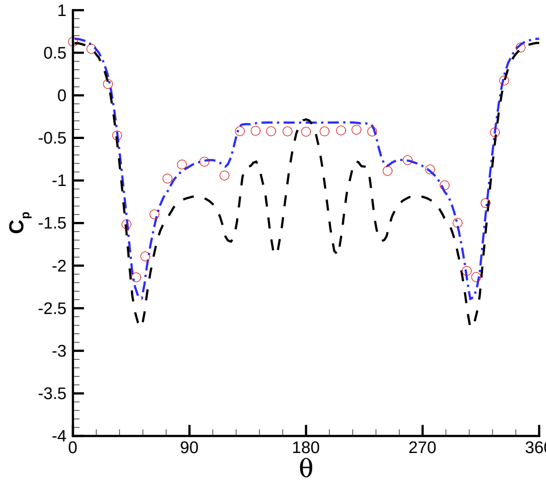

Fig. 8 Pressure coefficient at $x/L = 0.111$. **∘ measurements; —·— DES; ---- URANS.**

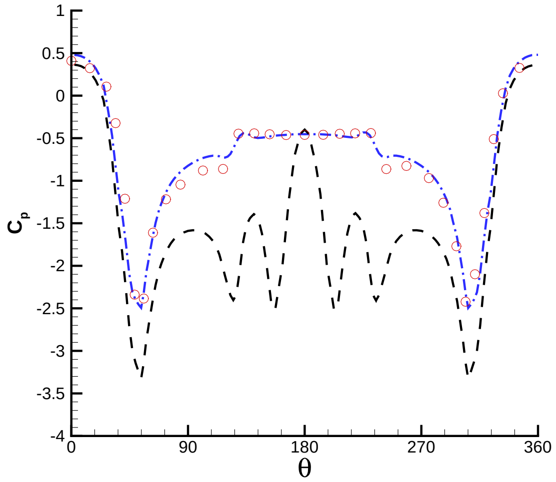

Fig. 7 Pressure coefficient at $x/L = 0.055$. **∘ measurements; —·— DES; ---- URANS.**

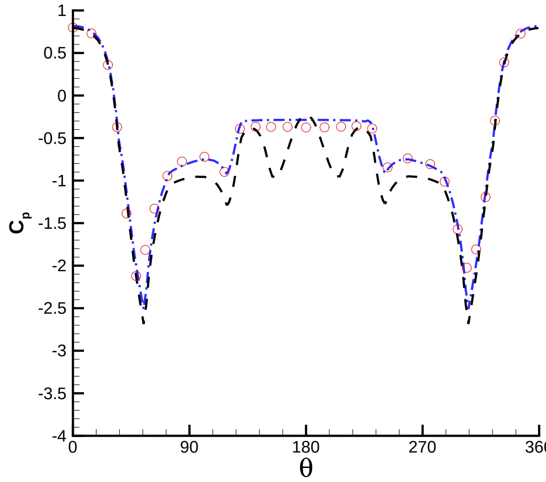

Fig. 9 Pressure coefficient at $x/L = 0.166$. **∘ measurements; —·— DES; ---- URANS.**

On the aftbody, Figures 12 and 13, the DES and RANS over-predict C_p near $\theta = 90°$ and $\theta = 270°$ at $x/L = 0.805$, but are otherwise accurate. Similarly, at the last axial station, the DES prediction is in slightly better agreement with the measured distribution than the RANS, though both techniques yield reasonable C_p. Compared to the axial stations along the forebody, the flow that develops over the endcap is complex, with a structure that yields more variation with θ than observed along the forebody.

For the ogive experiencing rotary motion at a spin coefficient of 0.2, contours of the instantaneous vorticity magnitude at three axial planes along the ogive are shown in Figure 15. The upper frame is on the forebody section at $x/L = 0.222$, the middle frame corresponding to $x/L = 0.5$, and the lower frame at $x/L = 0.805$. The influence of rotary motion on the vorticity shed into the wake is apparent, with the skewing towards opposite sides on the front and rear portions of the body as dictated by the local conditions.

DES predictions of the pressure distribution along the forebody at four axial stations are shown in Figures 16-19. Analogous to the behavior observed in the vorticity contours in Figure 15, pressure distributions show the influence of the rotary motion and are no longer symmetric about $\theta = 0°$. The minimum C_p occurs in the vicinity of the rear windward corner (relative to the induced velocity normal to the freestream flow).

Figure 16 shows that at $x/L = 0.111$ the minima in C_p near the windward corners are adequately recov-

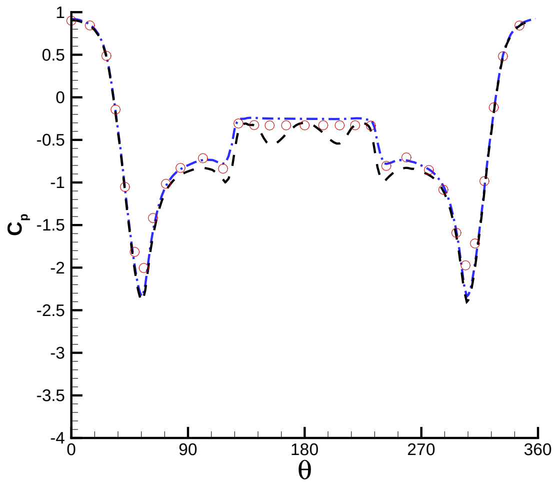

Fig. 10 Pressure coefficient at $x/L = 0.222$. ○ measurements; —·— DES; - - - - URANS.

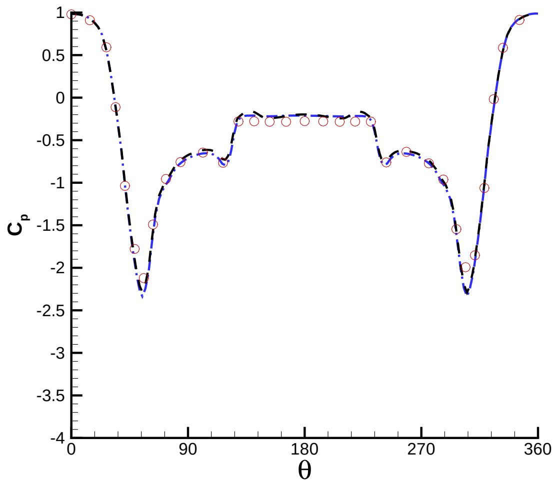

Fig. 11 Pressure coefficient at $x/L = 0.305$. ○ measurements; —·— DES; - - - - URANS.

ered, in addition to the relatively flat distribution on the lee side. The figure also indicates, however, that flow separation does not occur on the "rear" vertical surface in the measured case, while the DES prediction does experience separation, leading to the mismatch for $180° \leq \theta \leq 270°$. At $x/L = 0.166$, shown in Figure 18, the agreement between DES predictions and the measured pressure distribution is good, the minima in C_p around both windward corners is recovered, the DES result for the region with the most negative C_p improved compared to that at $x/L = 0.111$.

Pressure distributions at the last two axial stations along the forebody are shown in Figures 18 and 19. Both stations show very good agreement between DES predictions and the measured values. The measurements indicate attached flow around the windward

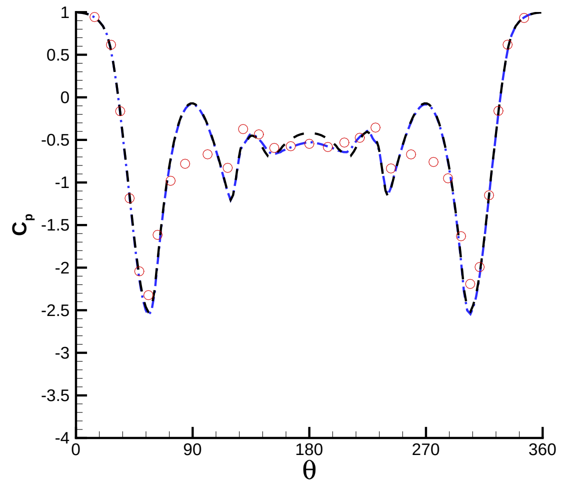

Fig. 12 Pressure coefficient at $x/L = 0.805$. ○ measurements; —·— DES; - - - - URANS.

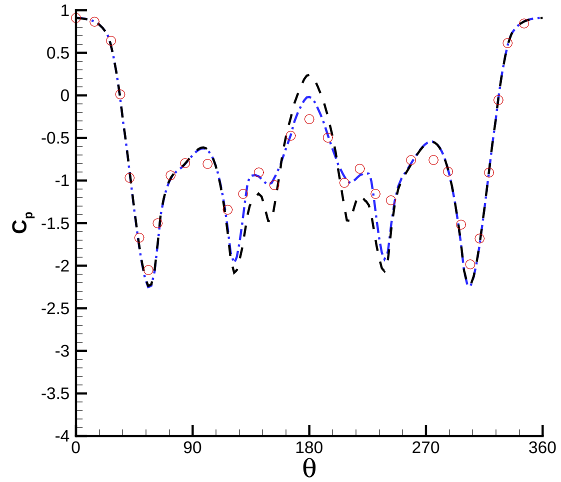

Fig. 13 Pressure coefficient at $x/L = 0.903$. ○ measurements; —·— DES; - - - - URANS.

corners with flow separaration on the lee side. The DES also predicts attached flow around the windward corners and in addition accurately captures the secondary minima induced by the interaction of the boundary layer with the leeward corners of the ogive. The uniform distribution along the leeward side in the separated region is also accurate.

Summary

DES predictions of the pressure distribution for the static-geometry and ogive undergoing rotary motion are relatively accurate. For the static-geometry case, DES is far superior to the result obtained using unsteady RANS. For the ogive at 90° angle of attack, URANS predictions of the flow in the wake region are overly coherent, the flow is characterized in the present

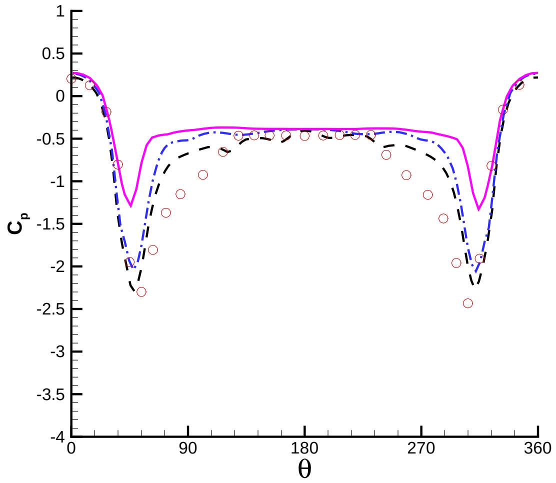

Fig. 14 Effect of grid refinement on the pressure coefficient at $x/L = 0.027$. ∘ measurements; —— coarse grid; —·— baseline grid; ---- fine grid.

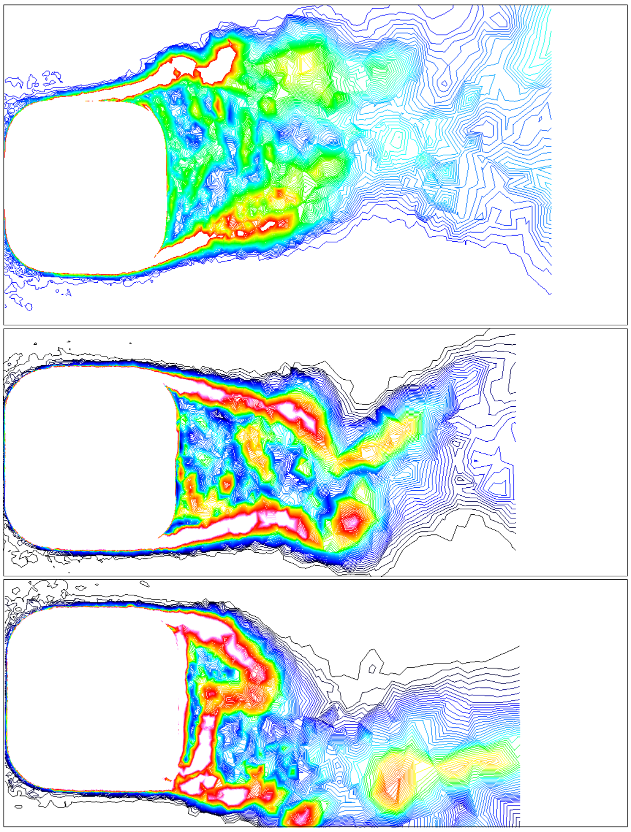

Fig. 15 Contours of the instantaneous vorticity in three axial planes for DES prediction of the flow with rotary motion. Upper frame: $x/L = 0.222$; middle frame: $x/L = 0.5$; lower frame: $x/L = 0.805$.

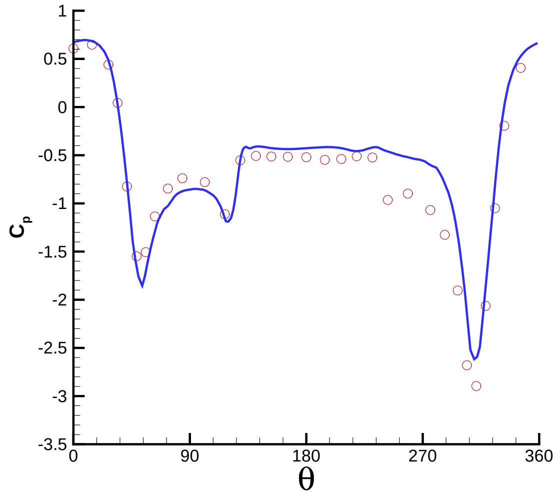

Fig. 16 Pressure coefficient at $x/L = 0.111$, spin coefficient, $\Omega L/(2U_\infty) = 0.2$. ∘ measurements; —— DES.

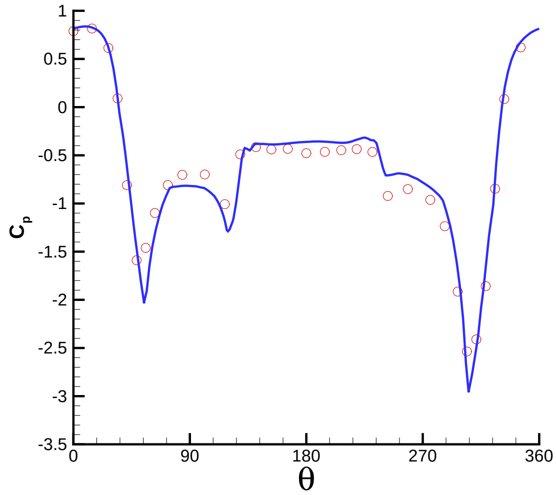

Fig. 17 Pressure coefficient at $x/L = 0.166$, spin coefficient, $\Omega L/(2U_\infty) = 0.2$. ∘ measurements; —— DES.

investigations by a strong pair of counter-rotating vortices. Strong three-dimensionality along the forebody is not recovered in the URANS, leading to a pressure distribution that has substantial variation in the separated region, rather than the uniform distribution measured in the experiments reported by Pauley *et al.* [5] and predicted in the DES.

Rotary motion was computed using an ALE formulation, applied to the ogive for the present investigations for rotation about the model center at a spin coefficient of 0.2. Visualizations of the vorticity magnitude in the leeward region showed the skewing of the wake by the rotation. Pressure distributions on the forebody exhibit adequate agreement with mea-

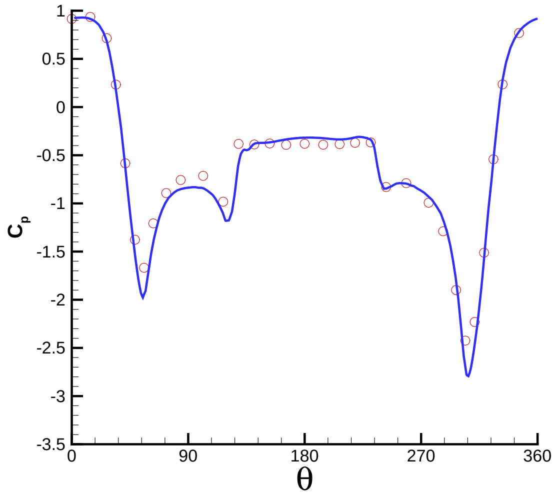

Fig. 18 Pressure coefficient at $x/L = 0.222$, spin coefficient, $\Omega L/(2U_\infty) = 0.2$. ∘ measurements; —— DES.

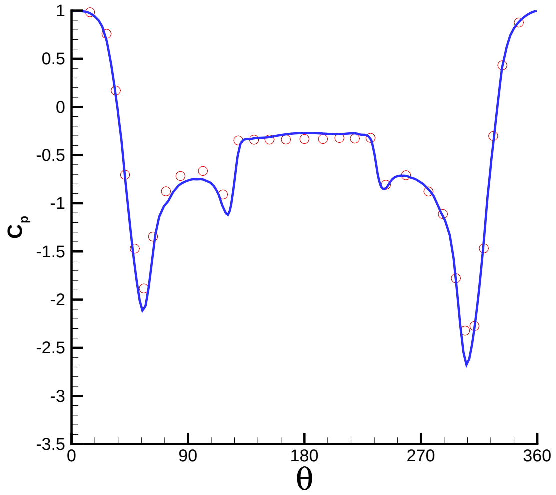

Fig. 19 Pressure coefficient at $x/L = 0.305$, spin coefficient, $\Omega L/(2U_\infty) = 0.2$. ∘ measurements; —— DES.

sured values, the asymmetry induced by the rotation being recovered and the overall variation with θ being accurately captured.

DES predictions of the static geometry were obtained for a range of mesh resolutions, the calculations showing that a deeper structure is resolved in the wake. This is an important attribute for hybrid RANS/LES methods, demonstrating that in the limit of very fine grids the role of the turbulence model would vanish and the technique approaches Direct Numerical Simulation. In general, the three-dimensionality of the wake was substantially stronger in the DES as compared to the RANS, consistent with related studies [12]. Though the wake structure did not exhibit as much axial (spanwise) variation in the URANS results, three-dimensionality was present, an aspect that probably contributes to the relatively accurate streamwise force prediction (as assessed against the DES result).

The present computations were performed of the flow with fully turbulent boundary layers, accomplished by seeding the inflow condition with a small level of eddy viscosity, sufficient to activate the turbulence model as the fluid entered the boundary layer. Measurements at lower Reynolds numbers showed strong *Re* effects[5] and such regimes comprise an important and challenging test case for hybrid methods. Effects of transition to turbulence, possibly intermingled with boundary layer separation, are exceedingly difficult to model and accuracy requirements are typically very high.

Finally, aircraft forebodies are often asymmetric due to imperfections in the geometry, an effect that can produce a large yawing moment, even for configurations without sideslip. The strong yawing moment on low aspect ratio aircraft such as the F-15E can lead to relatively flat spins, for example. The computational methodologies under development and assessment in this work, while not fully complete, will be important for accurately modeling such phenomena.

Acknowledgments

The authors gratefully acknowledge the support of the Air Force Office of Scientific Research (GrantF49620-02-1-0117, Program Officers: Dr. Thomas Beutner and Dr. John Schmisseur). The calculations were performed at the Maui High Performance Computing Center.

References

[1] Spalart, P. R. , Jou W-H. , Strelets M. , and Allmaras, S. R., "Comments on the Feasibility of LES for Wings, and on a Hybrid RANS/LES Approach," *Advances in DNS/LES, 1st AFOSR Int. Conf. on DNS/LES*, Aug. 4-8, 1997, Greyden Press, Columbus Oh.

[2] Spalart, P.R., and Allmaras, S.R., " A One-Equation Turbulence model for Aerodynamic Flows", *La Recherche Aerospatiale*, **1**, pp. 5-21, 1994.

[3] Strelets, M., "Detached Eddy Simulation of Massively Separated Flows", *AIAA Paper 2001-0879*, 2001.

[4] Forsythe, J.R., Wentzel, J.F., Squires, K.D., Wurtzler, K.E., Spalart, P.R., "Computation of Prescribed Spin for a Rectangular Wing and for the F-15E Using Detached-Eddy Simulation", *AIAA Paper 2003-0839*, 2003.

[5] Pauley,H., Ralston, J. and Dickes, E., "Experimental Study of the Effects of Reynolds number

on high Angle of Attack Aerodynamic Characteristics of Forebodies during rotary motion", NASA CR 195033, 1995.

[6] van Dam, C.P., Saephan, S., Fremaux, C.M. and DalBello, T., "Prediction of Flows about Forebodies at high Angle of attack Dynamics Conditions". Presented at NATO/RTO Applied Vehicle Technology Panel Symposium on Advanced Flow Management: Vortex Flow and High Angle of Attack, May 7-10, 2001, Leon, Norway. Paper No: MP-96-P39.

[7] Shur, M., Spalart, P. R., Strelets, M., and Travin, A, "Detached-Eddy Simulation of an Airfoil at High Angle of Attack, 4th Int. Symp. Eng. Turb. Modelling and Measurements, Corsica, May 24-26, 1999.

[8] Strang, W. Z., Tomaro, R. F. and Grismer, M. J., "The Defining Methods of Cobalt$_{60}$: a Parallel, Implicit, Unstructured Euler/Navier-Stokes Flow Solver," *AIAA 99-0786*, 1999.

[9] Gottlieb, J.J. and Groth, C.P., "Assessment of Riemann solvers for unsteady one-dimensional inviscid flows of perfect gases", *J. Comp. Physics*, **78**, pp. 437-458, 1998.

[10] Karypis, G., Schloegel, K., and Kumar, V, *ParMETIS: Parallel Graph Partitioning and Sparse Matrix Ordering Library Version 1.0*. University of Minnesota, Department of Computer Science, Minneapolis, MN 55455, July 1997.

[11] Pirzadeh, S., "Three-dimensional Unstructured Viscous Grids by the Advancing Layers Method", *AIAA J.*, **34**, pp. 43-49, 1996.

[12] Travin, A., Shur, M., Strelets, M. and Spalart, P.R., "Detached-eddy simulations past a circular cylinder", *Flow, Turbulence, and Combustion*, **63**, pp. 293-313, 2000.